Available online at www.sciencedirect.com
SCIENCE DIRECT
Catalysis Today 116 (2006) 289–297
CATALYSIS TODAY
www.elsevier.com/locate/cattod

Hydrogen production via CH_4 pyrolysis: Regeneration of ex hydrotalcite oxide catalysts

R. Guil-López *, V. La Parola, M.A. Peña, J.L.G. Fierro

Instituto de Catálisis y Petroleoquímica, CSIC, Marie Curie 2, Cantoblanco, 28049 Madrid, Spain

Available online 20 July 2006

Abstract

Pure hydrogen was obtained by catalytic methane decomposition over thermally stable nickel-based catalysts prepared from hydrotalcite-like precursors. Two different Ni–Mg–Al catalyst compositions were tested in the catalytic pyrolysis reaction of methane. The catalytic results were compared with those of a catalyst prepared by conventional impregnation of Ni–Mg phases on an alumina support. The high thermal stability of these catalysts was demonstrated in several reaction–regeneration cycles. The regeneration processes were performed with CO_2 and O_2 as regenerating agents. Using either CO_2 or O_2 gas, hydrogen production after regeneration increased with regard to the fresh catalyst. Upon catalyst regeneration, larger amounts of hydrogen were obtained on catalysts regenerated with CO_2 than with O_2. The high thermal stability of the Ni particles of the catalysts from hydrotalcite-like precursors was improved in the presence of Mg. This high Ni-stability is a key factor for increasing hydrogen production after consecutive reaction–regeneration cycles.

Keywords: Methane pyrolysis; Nickel catalysts; Hydrotalcite precursors; Regeneration

1. Introduction

The environmental pollution produced by the delivery of massive energy through the combustion of fossil fuels has made it necessary to develop new options based on sustainable sources. As an energy carrier, hydrogen (H_2) is an attractive choice, since it affords a clean energy when used either directly or as fuel in H_2-air fuel cells. Both concepts are considered as offering the major sources of clean energy in future decades [1]. Apart from these advantages, there are currently two major hurdles to be overcome in order to give hydrogen a major role in the energy sector: (i) existing hydrocarbon fuels are readily available and cheap, (ii) hydrogen, which is not really a primary fuel, must be produced from other primary sources with no significant cost in energy or pollution. In order to meet H_2 energy needs worldwide, its production must be considered within the framework of all resources available, including fossil fuels, in the near future of the so-called ''hydrogen economy'' [2]. In this way, the steam reforming of hydrocarbons [3], specifically of natural gas [3,4], is currently the largest and most economic way to produce hydrogen. Alternative ways include the partial oxidation of methane [3,5], the autothermal methane oxi-reforming reaction [6] and the dry reforming reaction of methane [3,7].

A different alternative route for hydrogen production is catalytic methane decomposition: so-called methane pyrolysis or methane decarbonization [3,8] (1).

$$CH_4 \rightarrow C + 2H_2, \qquad \Delta H^0 = +90.1\,\mathrm{kJ/mol} \tag{1}$$

This reaction has received much attention in recent years [9], because its most important characteristic is the production of H_2 free of CO or CO_2 and the only by-product of this reaction is a carbon material or a carbonaceous species [10]. The CO–CO_2-free H_2 produced is optimal for direct supply to a fuel cell, whose electrocatalysts are highly sensitive to the presence of CO at ppm levels in the hydrogen stream [11].

It is well documented that nickel catalysts catalyze the decomposition of methane into hydrogen and carbon as C-nanofibers [12,13]. The main problem of using Ni-catalysts is deactivation of the catalyst through the carbon deposits on the catalyst surface, over the Ni active centre [14]. Catalyst deactivation may be overcome by regeneration of the catalyst.

* Corresponding author. Tel.: +34 91 585 4759; fax: +34 91 585 4760.
E-mail address: rut.guil@icp.csic.es (R. Guil-López).

0920-5861/$ – see front matter © 2006 Elsevier B.V. All rights reserved.
doi:10.1016/j.cattod.2006.05.078

This carbon is in fact highly reactive to O_2 [15] (2) or CO_2 [16] (3):

$$C + O_2 \rightarrow CO_2, \qquad \Delta H^0 = -394.7\,\text{kJ/mol} \tag{2}$$

$$C + CO_2 \rightarrow 2CO, \qquad \Delta H^0 = +174.5\,\text{kJ/mol} \tag{3}$$

The use of CO_2 as a regenerating agent (reaction (3)) allows collection of the CO product, which can be considered as a useful intermediate chemical for carbonylation reactions of methanol and acetylene, the hydroformylation of alkene, the synthesis of phosgene or the formation of metal carbonyls [16].

On the other hand, the need for a regeneration process makes it necessary to use Ni-catalysts in which Ni crystallites have been stabilized in order to avoid Ni sintering during the regeneration process. An alternative option for stabilising active metal particles is the use of different precursors. The so-called hydrotalcite-like compounds seem to be good precursor candidates for preparing stabilized Ni-catalysts because they can afford highly thermally stabilized mixed oxides upon treatment at high temperature (calcination treatment) [17]. Hydrotalcite-like compounds are layered double hydroxides (LDHs) derived from brucite layers with an ideal formula of $[M_{(1-x)}^{2+}\,M_x^{3+}\,(OH)_2]\cdot[A^{-n}]_{x/n}\cdot m\,H_2O$; in which M^{2+} and M^{3+} can be any divalent and trivalent metal cation capable of occupying the octahedral interstitial sites of a brucite-like sheet, which are positively charged due to partial substitution of the magnesium by trivalent cations. A^{-n} is almost all classical balancing exchange anion (NO_3^-, CO_3^{2-}, Cl^-), amongst the others [18]. Upon heating, these highly ordered hydrotalcite-like compounds form an amorphous mixture of metal oxides – $M^{2+}M^{3+}(O)$ – with a very small crystal size that are stable under thermal treatment. These mixed oxides show interesting properties, such as a high specific surface area, high active metal dispersion, a strong interaction between different metals in mixed oxides, and a controllable basic character of the calcined mixed oxides [17]. Moreover, they form small, thermally stable metal crystallites under reduction conditions [19]. Thus, very stable nickel-containing material may be prepared by using the hydrotalcite-type structure as the starting material. In this sense, reduced Ni–Al(O) mixed oxides from hydrotalcite-like precursors were successfully tested as catalysts in the methane decomposition reaction by Li et al. [12,20]. These authors studied Ni deactivation by carbonaceous deposits and the lifetime of the Ni–Al(O) mixed oxides from the hydrotalcite-like precursors during methane decomposition.

In this work, we studied different Ni, Mg–Al catalysts from LDH precursors used in two cycles of the methane decomposition reaction to produce hydrogen and also the regeneration of the deactivated catalyst. Thus, this contribution explores the influence of Mg on Ni-stability in the mixed oxide matrix during two severe cycles of methane decomposition after regeneration process of the catalyst using CO_2 as an effective regenerating agent. Comparison of these catalysts from hydrotalcite-like precursors is also made with a Ni-catalyst prepared by classical impregnation of an alumina substrate modified by magnesium.

2. Experimental

2.1. Catalyst preparation

The hydrotalcite-like precursors described in this study were prepared by co-precipitation by urea hydrolysis [21]. An aqueous solution (0.5 M) containing appropriate amounts of $NiCl_2{\cdot}6H_2O$ (active metal), $MgCl_2{\cdot}6H_2O$ (modifying divalent cation), and $AlCl_3{\cdot}6H_2O$ in the presence of urea (urea quantity = $3 \times \sum$mol of cations) as the precipitating agent were heated, controlling the temperature to obtain the desired precipitation pH value. The precipitate was aged in suspension at 90 °C for 48 h under stirring. The resulting solid was filtered, thoroughly washed with distilled water – until the filtered water pH was around 6 – and dried overnight at 80 °C. All precursors contained both chloride (Cl^-) and carbonate (CO_3^{2-}) as charge compensating anions. Chemicals and reagents were purchased from Aldrich.

Two different samples, depending on nominal composition, were obtained with two different Ni-loadings: (i) high Ni-loading (nominal composition in the molar ratio of cations: 58.0% Ni–15.0% Mg) NMA-I, (ii) low Ni-loading (18.0% Ni–46.0% Mg) NMA-II. The two LDH-precursors were calcined to obtain the corresponding mixed oxides under a flow of air in a temperature-programmed furnace. Temperature was increased from room temperature to 850 °C at a rate of 1 °C min^{-1} and maintained for 7 h. The Ni–Mg-supported catalyst (15% Ni/Al_2O_3–10% Mg) was prepared by sequential impregnation of a commercial α-alumina. The alumina powder was suspended in a solution containing the required amount of magnesium acetate. The excess of water was evaporated off to dryness in a rotary evaporator at 70 °C. The samples were then calcined in air at 850 °C for 4 h. The operation was then repeated with a solution of nickel acetate. The sample was labelled imp-NMA. A reference Ni–Al spinel ($NiAl_2O_4$) was prepared by a standard ceramic method, using the corresponding chloride salts at the desired amounts, and heated in air at 1000 °C for 10 h.

2.2. Catalyst characterization

Chemical analyses of the hydrotalcite-like precursors and their corresponding mixed oxides were carried out on an ICP-AES Perkin-Elmer Optima 3300 DV spectrometer. The textural properties of the catalysts were determined by N_2 adsorption isotherms, measured at the temperature of liquid nitrogen on a Micromeretics TRISTAR 3000 instrument. Prior to the adsorption measurements, the samples were degassed at 413 K overnight.

Powder X-ray diffraction (XRD) patterns of the hydrotalcite-like precursors and the corresponding mixed oxides were recorded on a Seifert 3000 P diffractometer, using nickel filtered Cu $K\alpha_1$ radiation and a scanning rate of 0.04° 2θ s^{-1}. The crystalline phases were identified by comparison with the Joint Committee on Powder Diffraction Standards (JCPDS) files [22]. Particle-size estimates for the calcined samples, reduced samples, and samples used in the reaction–regeneration cycles were calculated from the experimental line

broadening (linewidth at half maximum, FWHM) of the characteristic Ni reflection using the Debye–Scherrer equation.

X-ray photoelectron spectra (XPS) were acquired with a VG Escalab 200R spectrometer equipped with a hemispherical electron analyzer and an Mg Kα ($h\nu = 1253.6$ eV) X-ray source. The peaks were fitted by a non-linear least square fitting program using a properly weighted sum of Lorentzian and Gaussian component curves after background subtraction according to Shirley and Sherwood. The constant charging of the samples was corrected by referencing all energies to the Al 2p peak at 74.5 eV.

The TPR analyses were performed on a Micromeretics 2900 TPD/TPR instrument. The reducing agent was 10 vol.% H_2/Ar, gas flow 50 mL min^{-1}. The samples (35 mg) were heated from room temperature to 1000 °C at a rate of 10 °C min^{-1}. This heating program was chosen based on the literature to optimize the resolution of the curves. Calibration of the instrument was carried out with a CuO standard (from Merck). Several cycles of reduction-regeneration cycles were conducted with fresh catalysts to study Ni stabilization.

Two different thermogravimetric measurements were carried out on a Mettler Toledo TGA/SDTA 851 thermal analyser. The first type of experiment consisted of 10 cycles of reduction–reoxidation of fresh catalysts under conditions analogous to those of TPR analysis. The reduction process consisted of heating the samples (10 mg) from room temperature to 1000 °C under a 20 vol.% H_2/N_2 flow. After reduction, the sample was purged in N_2 to room temperature and was then re-heated up to 1000 °C under a 20 vol.% O_2/N_2 flow. The second type of thermogravimetric experiment consisted of testing the regeneration of the used catalyst efficiency. The regenerated catalysts – after reaction – were oxidized to quantify the amount of carbonaceous deposits by heating the used and regenerated catalysts from 50 to 1100 °C under an O_2/N_2 flow. Subsequently, the oxidized catalysts were reduced under analogous conditions to those of the TPR analysis.

2.3. Methane decomposition and catalyst regeneration

Temperature-programmed CH_4 decomposition was performed on 60 mg samples loaded in a U-shaped quartz reactor (4 mm i.d.) at atmospheric pressure on-line with a Baltzer Prisma QMS 200TM quadrupole mass spectrometer. Accelerated catalyst deactivation tests were chosen to probe catalyst stability. Prior to the reaction, the catalyst was reduced in a 10% H_2/Ar flow at 900 °C for 30 min. After reduction, the sample was purged in Ar to room temperature and then the reaction mixture (23% CH_4/Ar at a total flow of 65 mL min^{-1}) was introduced, and temperature was increased from 60 to 850 °C, at 10 °C min^{-1}. After the CH_4 pyrolysis reaction, the used deactivated catalysts were regenerated using either CO_2 or O_2 as the regenerating agent. A flow of 10% of regenerating agent/Ar (100 mL min^{-1}) was passed while heating to 700 °C or 600 °C, for CO_2 and O_2, respectively, maintaining the maximum temperature for 2 h. Thus, each cycle included three steps: (i) reduction, (ii) catalytic methane decomposition, (iii) catalyst regeneration—with CO_2 or O_2. For each catalyst, two cycles of three steps were completed. The main (m/z) signals relative to H_2, H_2O, CH_4, CO, CO_2 and Ar were recorded during the three steps of each of the two cycles of experiments. To eliminate errors due to changes in pressure within the ionization chamber of the spectrometer, all signals were referred to the Ar signal.

3. Results and discussion

3.1. General characterization

Chemical analysis of hydrotalcite-like precursors and the corresponding mixed oxides revealed no significant differences with the nominal composition. In order to determine whether or not cations were lost along the synthesis, filtered mother-liquor waters were also analysed. The result showed a small loss of Mg^{2+} (always less than 3%) in filtered mother-liquor waters (Table 1). Table 1 also shows some textural properties of the mixed oxides derived from LDH. The high values of the specific surface area of ex-LDH mixed oxides (NMA-I and NMA-II) point to the high thermal stability of the specific area in these mixed oxides pretreated at such a high temperature (850 °C for 7 h, under air flow) during the calcination process. In contrast, the supported catalyst (imp-NMA) displayed a very low surface area, characteristic of the alumina α-phase.

The powder X-ray diffraction patterns of the two non-calcined hydrotalcite-like precursors (Fig. 1) reveal a single phase typical of the hydrotalcite structure [17,23]. The basal reflections (0 0 3), (0 0 6) and (0 0 9) are easily recognized in the patterns of the hydrotalcite-like materials, although the (0 0 9) line overlaps the (0 1 2) and (0 1 5) reflections, resulting in a broad signal between 40° and 45° 2θ. No excess phase was detected, suggesting that Ni^{2+} had isomorphically replaced Mg^{2+} cations in the brucite layers. The relatively high intensities combined with broad lineshapes indicate a relatively high crystallinity of the hydrotalcites. LDH crystallinity increased with Ni content.

Thermal decompositions of LDH precursors were completed from the layered structure (Fig. 1) to oxide structures (Fig. 2) at 850 °C. The XRD pattern of Ni–Mg–Al mixed oxides from LDH (Fig. 2a and b) exhibited three broad reflections at about 37°, 44° and 63° 2θ, characteristic of the periclase MgO (JCPDS file no. 43–1022) and/or bunsenite NiO

Table 1
Chemical composition and textural properties of the calcined materials

Catalyst	Chemical composition[a]			Textural properties from N_2 adsorption	
	Ni	Al	Mg	BET surface area (m^2 g^{-1})	Average pore diameter (nm)
NMA-I	58	28	14	64	21
NMA-II	19	37	44	73	23
imp-NMA	15	75	10	4	46

[a] Chemical composition in atomic percentage of cations.

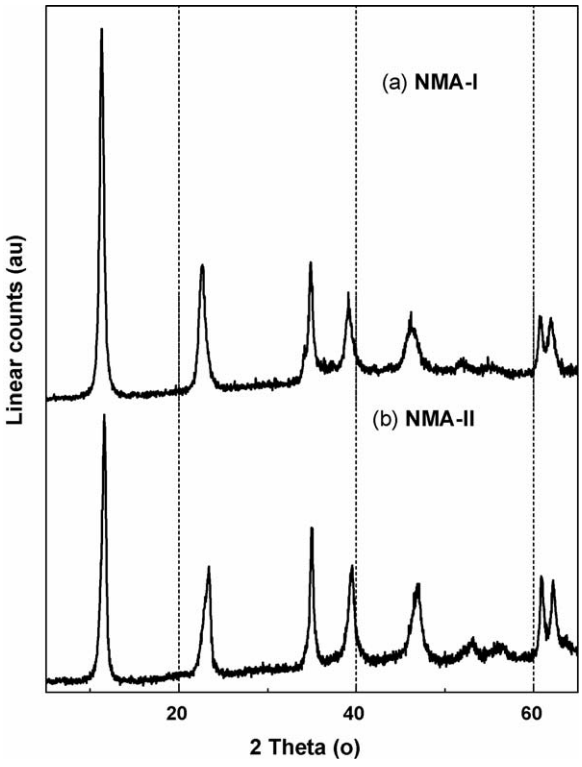

Fig. 1. XRD patterns of LDH precursors of Ni catalysts ex-LDH: (a) NMA-I (58% Ni–27% Mg–15% Al), and (b) NMA-II (19% Ni–37% Mg–44% Al).

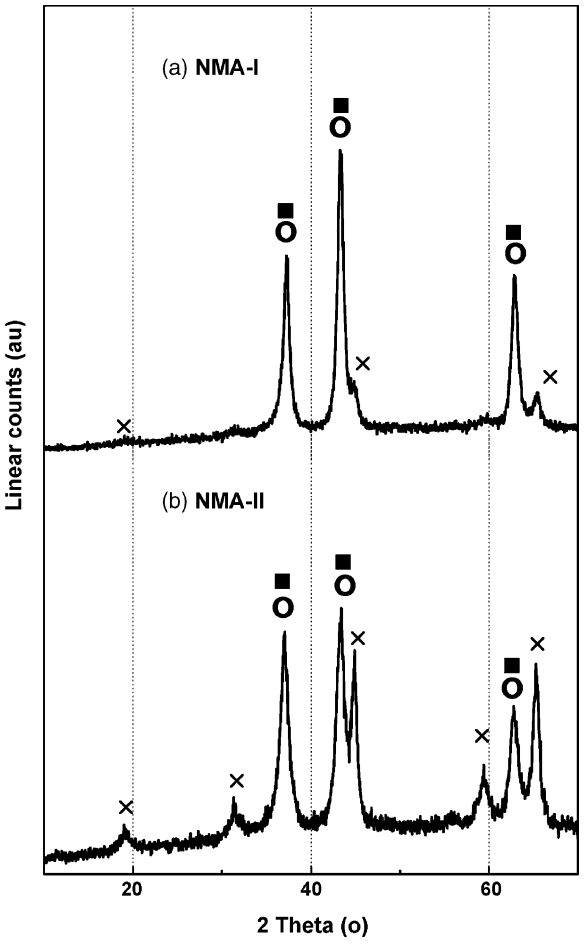

Fig. 2. XRD patterns of calcined Ni catalysts ex-LDH: (a) NMA-I and (b) NMA-II. Phase identification: (■), NiO; JPDF no. 22-1189; (○), MgO; JPDF no. 43-1022; (×), $NiAl_2O_4$; JPDF no. 78-552.

(JCPDS file no. 22–1189) phases. Owing to the almost complete coincidence of the diffraction lines of the MgO and NiO phases, discrimination among these phases was not possible. Additional weak peaks at about 19°, 32° and 45° 2θ can be attributed to the formation of spinel $Mg_xNi_{1-x}Al_2O_4$ phases, e.g. $NiAl_2O_4$ JCPDS file no. 78–552. The amount of spinel phases increased with increasing magnesium loading, from Fig. 2a (15% Mg) to Fig. 2b (46% Mg), but it was not possible to determine the chemical composition of the spinel phase by XRD.

The crystallite size of the segregated nickel oxide phase was obtained from the XRD line broadening (Table 2). To avoid the strong overlap of the most characteristic reflections of the MgO and NiO phases, the NiO (1 1 1) reflection at about 37° 2θ was considered because its intensity of 68% is much higher than the corresponding characteristic reflection of MgO (4%). Ex-LDH catalysts display a rather small crystal size of the NiO crystallites (cf. Table 2); however, a much larger crystallite size is derived from the imp-NMA sample, whose nickel-loading is similar to that of NMA-II. The large particle size of NiO crystallites in the imp-NMA sample is due to the low specific surface area of the α-alumina substrate, which causes a low interface to disperse nickel species. The crystallite size of the metallic nickel particles in the reduced samples and those used in the methane reaction are also shown in Table 2 (vide infra).

XP analyses of fresh catalysts and reduced NMA-I sample were performed to determine both the chemical state of the elements and the relative surface proportions in the catalysts. For each sample, Ni $2p_{3/2}$, Al 2p, Mg 2p, O 1s and C 1s core-level spectra were recorded. The binding energies of the principal peaks are summarized in Table 3; the percentages of the different peak contributions are given in parentheses. The binding energies for the Ni $2p_{3/2}$ level in both at 856.0 eV in

Table 2
Crystal size of segregated NiO and metallic Ni estimated using the Debye–Scherrer formula performed on fresh and reduced catalyst and that used in the reaction–regeneration process

Catalyst	Crystal size of treated samples (nm)			
	Calcined-fresh[a] (NiO)[b]	Reduced[c] (Ni)[b]	Used in reaction[d] (Ni)[b]	
			O_2[e]	CO_2[f]
NMA-I	8	13	–	–
NMA-II	6	11	8	7
imp-NMA	29	–	–	–

[a] Performed prior to reduction.
[b] Nature of the Ni particle measured.
[c] Performed on calcined and later reduced samples.
[d] Samples used in the CH_4 decomposition reaction.
[e] Regenerating agent used in the regeneration process: O_2. Last step: reaction process.
[f] Regenerating agent used in the regeneration process: CO_2. Last step: regeneration process.

Table 3
Binding energies (eV) of core electrons of the HT samples and surface atomic ratios of NMA-I and NMA-II fresh catalysts and reduced NMA-I

Catalyst	Ni $2p_{3/2}$ (%)	Ni/Al (nominal value)	Mg/Al (nominal value)
NMA-I fresh	856.5 (100)	2.50 (2.15)	0.38 (0.55)
NMA-II fresh	856.1 (100)	0.35 (0.5)	0.48 (1.3)
NMA-I reduced[a]	853.0 (31) 855.9 (69)	0.34	0.15

[a] Reduction process in the TPR equipment: 10% H_2/Ar (50 mL min^{-1}), heated from RT to 1000 °C at 10 °C min^{-1}.

ex-LDH fresh mixed oxides are assigned to Ni^{2+} in structures with strong interactions with the support [24]. The Ni/Al ratio derived for ex-LDH mixed oxides is close to the bulk Ni/Al ratio. This result confirms the homogeneous distribution of the cations in the mixed oxide derived from the LDH structure. The Ni $2p_{3/2}$ peak of the reduced NMA-I sample (Table 3) was deconvoluted into two contributions, at binding energies of 853.0 and 856.2 eV, which are usually assigned to zero-valence Ni^0 and Ni^{2+} species strongly interacting with the support, respectively [24]. On examining the peak percentages corresponding to the above components in the Ni $2p_{3/2}$ level (Table 3, in parentheses), it is clear that no complete reduction of metal was achieved. Passivation of the reduced Ni-catalysts may account for the observation of some oxidized nickel species.

3.2. Reduction studies

TPR experiments were carried out to study the reducibility of nickel oxide species on fresh and used catalysts. These TPR studies were conducted to test catalyst stability by monitoring both H_2 consumption and weight loss in the samples. The H_2 consumption profiles of the two ex-LDH samples, the imp-Ni, and the Ni-spinel ($NiAl_2O_4$) reference are shown in Fig. 3. All reduction temperatures and percentages of Ni reduced of the different deconvoluted peaks for each sample are shown in Table 4. High reduction temperatures were needed to reduce Ni^{2+} environments in all samples. All these reduction temperatures are substantially above 380 °C, which is the temperature for the reduction of bulk NiO, whose NiO crystallite size is close 35 nm. The high reduction temperatures, even above 1000 °C for imp-NMA (Fig. 3c), may be due to a strong Ni-support interaction or Ni^{2+} incorporation in a solid solution.

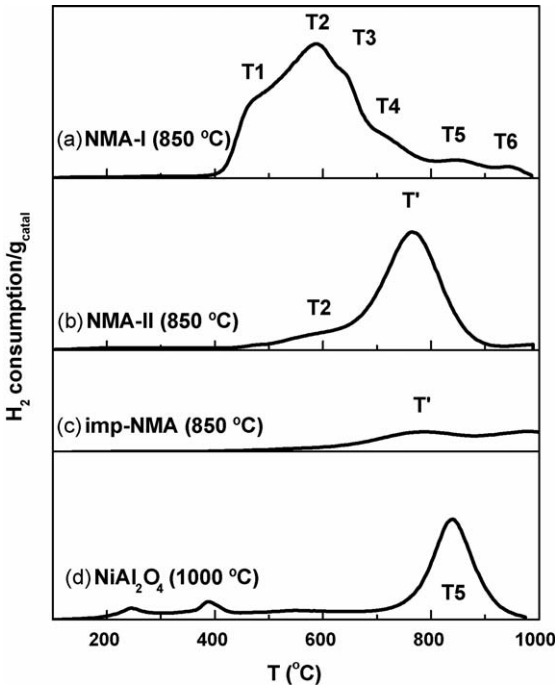

Fig. 3. TPR profiles of ex-LDH catalysts: (a) NMA-I; (b), NMA-II; (c) conventional impregnation imp-NMA, (d) Ni-spinel, $NiAl_2O_4$.

Fig. 3a shows the complex reduction profile for the NMA-I sample, with six (T1–T6) different Ni^{2+} environments (cf. Fig. 3a and Table 4). This complexity arises from the high Ni-loading in NMA-I, which causes several Ni^{2+} environments. In contrast, the lower Ni-loading in NMA-II determines a more homogeneous Ni^{2+} environment with the main peak (T′) and a shoulder almost coinciding with that of NMA-I (T2 in Table 4). The NMA-II main peak (T′) matches the main peak of imp-NMA (Table 4) and is close to the T5 peak, which is characteristic of the spinel phase (Fig. 3d). In sum, the reduction profiles of all the samples reveal different interactions between Ni^{2+} ions and the oxide substrate as well as the incorporation of Ni^{2+} ions in solid solutions.

To confirm the stability of the active phase (Ni), the ex-LDH catalysts were subjected to 10 reduction–oxidation cycles at high temperature, recording the weight changes of the samples in the thermobalance instrument. The reduction profiles-referred to weight loss-of a few number of cycles of the samples NMA-I and NMA-II are shown in Fig. 4. Significant differences among the samples were observed. Reduction temperature and the percentage of Ni reduced of the different deconvoluted peaks for each reduction profile for the first and

Table 4
Reduction temperature (°C) and percentage (%) of the deconvoluted peaks of the reduction profiles of the NMA-I and NMA-II samples and the reference samples imp-NMA and Ni-spinel

Catalyst	T1	T2	T3	T4	T′	T5	T6	T″
NMA-I fresh	470 (19%)	580 (40%)	650 (30%)	720 (6%)	–	850 (3%)	950 (2%)	–
NMA-II fresh	–	570 (7%)	–	–	770 (93%)	–	–	–
imp-MNA	–	–	–	–	775[a]	–		>1100[a]
Ni-spinel	–	–	–	–	–	840 (97%)	–	–

[a] Final reduction temperature up to 1100 °C; no determination of percentage of Ni reduced.

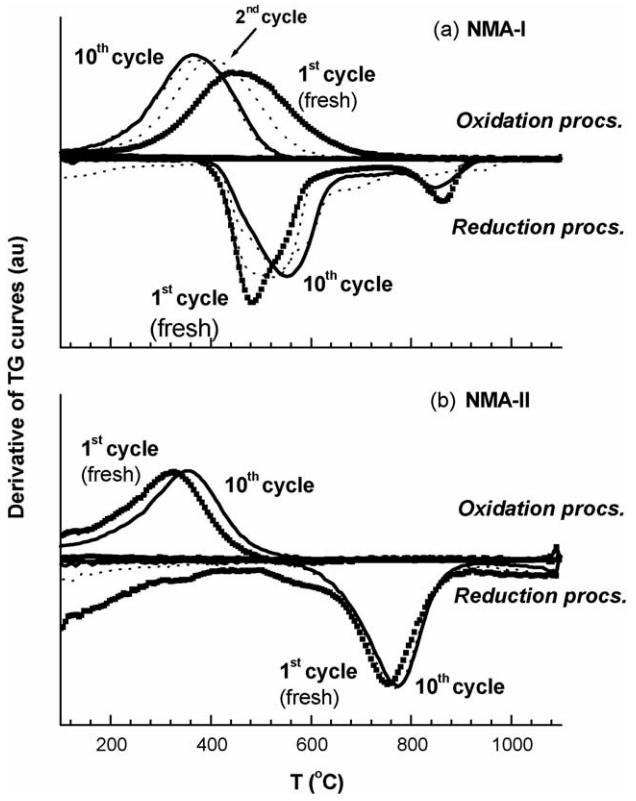

Fig. 4. Studies of reduction–reoxidation cycles of (a) NMA-I (10 cycles) and (b) NMA-II (10 cycles), using the TG technique. The positive DTG curve corresponds to oxidation processes and the negative DTG curve corresponds to reduction processes. First cycle (squares), last cycle (solid line), and intermediate cycles (dotted lines).

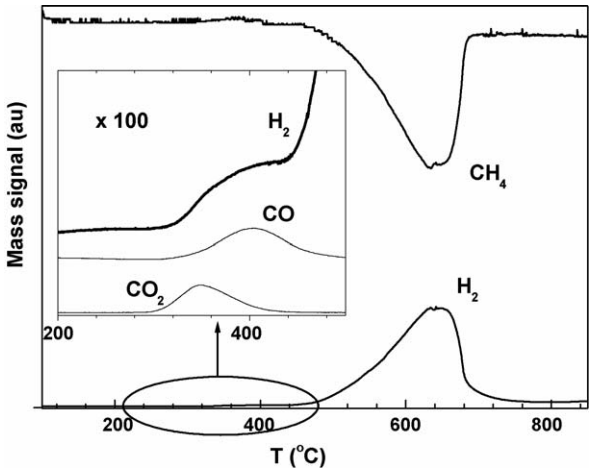

Fig. 5. Results of catalytic methane pyrolysis on the NMA-II sample. The corresponding results to CH_4 consumption and H_2 production are represented by their corresponding (m/z) mass profiles as a function of temperature. The CO and CO_2 profiles have been enlarged for to facilitate identification. All mass signals were referred to the Ar signal.

the last cycles are shown in Table 5. The most stable catalyst was the one with low Ni-loading (NMA-II), which maintained its reduction profile during the 10 reduction–reoxidation cycles (Fig. 4b). In this catalyst, the Ni^{2+} environment stabilized reduced Ni species at high temperatures through interaction of the reduced Ni particles with the mixed oxide matrix. The only change in NMA-II is the disappearance of the shoulder present at lower temperature (T2 peak, Table 5). The disappearance of the T2 peak may due to the incorporation of Ni^{2+} inside the mixed oxide matrices.

For the NMA-I sample, no change in the reduction temperature was observed although Ni distribution was altered to a certain extent (cf. Fig. 4a and Table 5). The lower temperature peak (T1) increased at the expense of the T2 and T3 peaks, but T3 maintained its Ni-population at the expense of the T4 peak, which disappeared (cf. Table 5). Peak T6 also disappeared while the T5 peak increased. The increase in the background at high temperature during the last cycle indicates that the transformation has not yet concluded (Fig. 4a). Finally, all 10 oxidation profiles were also different for each catalyst (Fig. 4), pointing out that different Ni environments are maintained after reduction.

3.3. Methane decomposition and catalyst regeneration

The results for catalytic methane pyrolysis on the NMA-II catalyst are shown in Fig. 5. The results corresponding to CH_4 consumption and H_2 production are expressed in terms of the corresponding (m/z) mass spectra as a function of temperature. The only products detected were hydrogen and traces of carbon oxides. Fig. 5 (inset) shows the low amount of CO_x produced (note the 100-fold smaller scale of the CO_x signal). The CO_x produced comes from the initial C deposits produced at low temperature (cf. Fig. 5: H_2 begins to appear about 315 °C), which react with the most reactive oxygen from the catalyst surface. It is known that increasing support basicity can lead to the promotion of carbon gasification [25]. When this small quantity of highly reactive oxygen is fully depleted, no more CO_x is detected. A good correlation between CH_4 consumption and H_2 production was found. Methane consumption and

Table 5
Reduction temperature (in °C) and percentage (%) of the deconvoluted peaks of the reduction profiles of the fresh NMA-I and NMA-II samples, and the same samples after 10 cycles of reduction–reoxidation derived from TGA

Sample	T1	T2	T3	T4	T′	T5	T6
NMA-I fresh	460 (19%)	550 (39%)	595 (24%)	660 (8%)	–	840 (7%)	940 (3%)
NMA-I after 10 cycles	460 (47%)	540 (19%)	630[a] (22%)	–	–	855 (12%)	–
NMA-II fresh	–	570 (10%)		–	750 (90%)	–	–
NMA-II 10 cycles	–	–	–	–	760 100%	–	–

[a] The FWHM of this peak was 350 °C *vs.* an average of 70 °C of other peaks, indicating that several species reducing in the large temperature range were present.

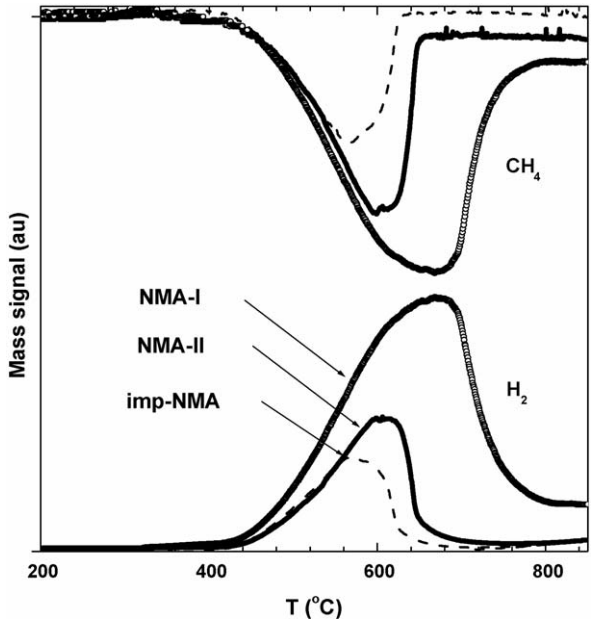

Fig. 6. Results of catalytic methane pyrolysis on the catalysts: (circles) NMA-I; (solid line) NMA-II, (dotted line) imp-NMA. CH_4 and H_2 mass signals were monitored for each catalyst. All mass signals were referred to the Ar signal.

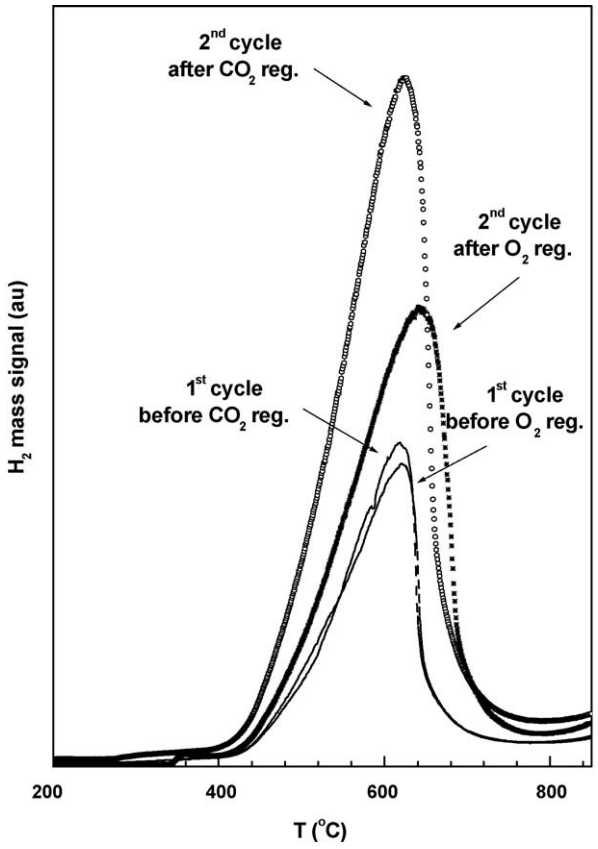

Fig. 7. H_2 produced from catalytic methane pyrolysis on NMA-II along the first reaction cycle before O_2 or CO_2 regeneration (dashed line); the second cycle after CO_2 regeneration (circles); and the second cycle after O_2 regeneration (dotted line). H_2 production is represented by the corresponding (m/z) mass as a function of temperature. All mass signals were referred to the Ar signal.

subsequent hydrogen production showed a maximum value after which activity decreased at temperatures higher than 700 °C (Fig. 5). The asymmetry of the CH_4 or H_2 mass signal curves is due to the abrupt deactivation of the catalyst by C deposition. The drop in activity parallels reactor plugging as a consequence of carbon accumulation.

Fig. 6 compares the results for catalytic methane pyrolysis on the three catalysts studied: NMA-I, NMA-II and imp-NMA. For all catalysts, the main product was H_2 and smaller quantities of CO_x. Deactivation occurred in all cases. The hydrogen produced before complete deactivation and the temperature of maximum hydrogen production depended on the nature of the sample (Table 6). Since the most active catalyst was the one with higher Ni-loading (NMA-I), a larger amount of carbon deposit was needed to completely deactivate all exposed Ni atoms. However, to qualitatively compare the total H_2 produced per Ni contents for all catalysts, it can be observed that this value was almost the same for the two ex-LDH catalysts [NMA-I (8.5) and NMA-II (9.0)] and lower for the imp-NMA (6.5). For a similar Ni-loading, the NMA-II catalyst was more active than the imp-NMA (cf. Table 6 and Fig. 6). Two reasons can be involved to explain this difference in activity: (i) the smaller Ni-crystal size of NMA-II (Table 2), with more exposed Ni atoms, requires a larger proportion of carbonaceous residues to completely deactivate all Ni atoms, (ii) TPR studies (Fig. 3c and Table 4) revealed that imp-NMA required a higher reduction temperature than the one used in the catalytic studies (900 °C).

The NMA-II sample was chosen to study the stability of Ni during the regeneration process. The intermediate activity of this catalyst is optimal for studying small differences between the two regenerating agents used, and NMA-II proved to be the most stable catalyst, as demonstrated by the reduction–

Table 6
Activity results for the decomposition of methane using the NMA-I, NMA-II and imp-NMA catalysts

Catalysts	Catalytic activity		Temperatures (°C)		
	CH_4 conversion[a] (%)	Total H_2 produced (a.u.)[b]	Start H_2 production[c]	Maximum activity	Deactivation
NMA-I	48	30	460	650	680
NMA-II	39	10	480	600	625
imp-MNA	25	6	480	565	590

[a] Maximum value.
[b] Integral of Ar-normalized H_2 mass signal curve.
[c] CH_4 conversion about 5%.

reoxidation cycles (Table 5, Fig. 4). To check the deactivation of the catalyst, two reaction cycles were carried out without performing the regeneration process between the cycles (results not shown). After the first reaction cycle (fresh catalyst), the NMA-II catalyst became deactivated, and no-activity was observed in the following cycles of methane decomposition. Fig. 7 shows the hydrogen produced using: (i) fresh NMA-II catalyst (1st reaction cycle), (ii) CO_2-regenerated NMA-II catalyst (2nd cycle-CO_2), (iii) O_2-regenerated NMA-II catalyst (2nd cycle-O_2). Good reproducibility of the reaction system was seen, as can be observed for the same evolution of the hydrogen produced during the two first cycles of methane decomposition (Fig. 7). In terms of the amount of hydrogen produced, regeneration with CO_2 proved to be better than with O_2. Nonetheless, both regenerated NMA-II catalysts were more active than the fresh counterpart (Fig. 7). The higher activity of the regenerated catalysts may be explained in terms of the re-dispersion of Ni particles during the reaction and regeneration processes [26]. Fig. 8 shows the reduction profiles of NMA-II during the reaction–regeneration studies. When O_2 was used as regenerating agent (Fig. 8a), a decrease in the Ni reduction temperature was observed. This decrease indicates Ni particle re-dispersion, as measured by XRD (Table 2) of the used catalyst, and this is a common trend in supported catalysts. When CO_2 was used in catalyst regeneration (Fig. 8b), no reduction of the used-regenerated catalysts was observed. The oxidation power of CO_2 was insufficient to oxidize the Ni metallic particles. Nickel particle size of the CO_2 regenerated sample decreased with respect to the sample after the first reduction (Table 2), indicating re-dispersion of the Ni particles after CO_2 regeneration. Despite this, the size of the Ni particles after CO_2 or O_2 regeneration was almost the same (Table 2). It has been proposed that deposited C may also be active for methane pyrolysis [27]. On the other hand, dilution of the deposited C in the Ni particles produces nickel carbide formation [28]. It is possible that nickel carbide might be more active for catalytic methane decomposition than metallic Ni. Unfortunately, the XRD nickel carbide pattern coincided with the metallic Ni pattern. Both hypotheses imply the involvement of carbon, although oxygen must play an important role in the new active phase of the catalyst because deposited C deactivated the catalyst and hence oxygen, from O_2 or CO_2, must be required to reactivate the catalyst.

To gain information about the nature of the new active site after regeneration processes, the oxidation and subsequent reduction of the CO_2-regenerated NMA-II catalyst was carried out (Fig. 9). Fig. 9a shows that most of the Ni was present as metal in the regenerated catalyst, although there was another fraction of Ni oxide. When this oxidised-regenerated catalyst was reduced again (Fig. 9b), only 75% of the metallic Ni was reduced, and the rest (25%) of the Ni remained unreduced. The high oxidation temperature (cf. Fig. 9, 1100 °C), which is sufficient for the oxidation of Ni and nickel carbide in other nickel-containing catalysts [29], did not allow the reduction of this fraction of nickel oxide.

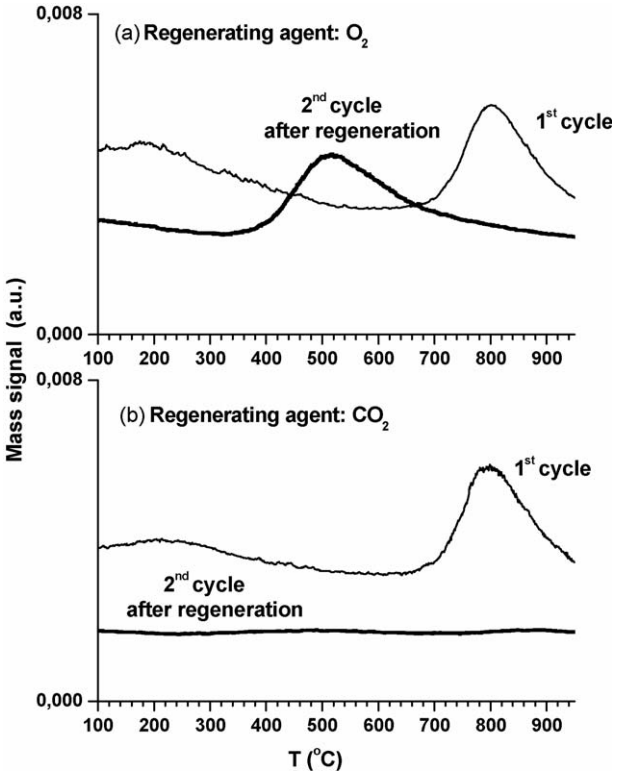

Fig. 8. Reduction processes during the reduction steps after regeneration with (a) O_2 or (b) CO_2, as regenerating agents. First reduction of the fresh NMA-II and second reduction of the regenerated NMA-II sample are represented by solid line and squares, respectively. Reduction represented by corresponding (m/z) mass of H_2O produced as a function of temperature. All mass signals were referred to the Ar signal.

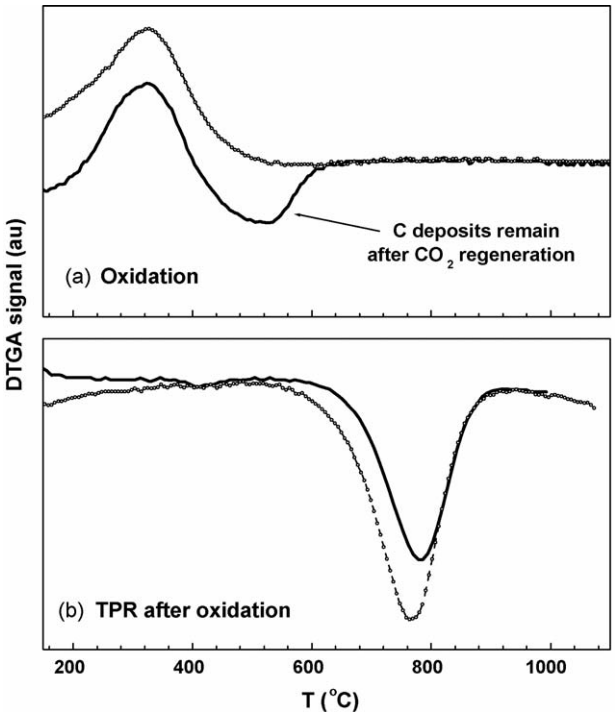

Fig. 9. (a) Oxidation of reduced fresh NMA-II (dash line) and CO_2-regenerated used NMA-II catalyst (solid line). (b) Reduction of fresh NMA-II (dashed line) and re-oxidized NMA-II after CO_2 regeneration (solid line).

4. Conclusions

Ni-containing hydrotalcite-type precursors subjected to calcination and activation are promising candidates for the production of hydrogen by catalytic methane decomposition. These systems were seen to display high thermal stability, as demonstrated by their performance along several reaction–regeneration cycles. The deactivating carbonaceous deposits produced along the pyrolysis process were removed, at least in part, by a consecutive oxidation cycle involving O_2 or CO_2. Both regeneration methods are very effective, since the re-dispersion of the metallic nickel produced during the oxidation phase increased catalytic activity. This effect was more important in the case of CO_2, which did not re-oxidise the nickel during regeneration and may prevent oxidation of the active nickel carbides formed during the methane decomposition reaction.

References

[1] S.S. Penner, Energy 31 (2006) 33–43.
[2] J.N. Armor, Catal. Lett. 101 (2005) 131–135.
[3] M.A. Peña, J.P. Gomez, J.L.G. Fierro, Appl. Catal. A: Gen. 144 (1996) 7–57.
[4] V.R. Choudhary, S. Banerjee, A.M. Rajput, Appl. Catal. A: Gen. 234 (2002) 259–270.
[5] (a) J. Barbero, M.A. Peña, J.M. Campos-Martin, J.L.G. Fierro, P.L. Arias, Catal. Lett. 87 (2003) 211–218;
(b) I. Aartun, B. Silberova, H. Venvik, P. Pfeifer, O. Gorke, K. Schubert, A. Holmen, Catal. Today 105 (2005) 469–478.
[6] P.M. Torniainem, X. Chu, L.D. Schmiddt, J. Catal. 146 (1994) 1–10.
[7] L.M. Cornaglia, J. Munera, S. Irusta, E.A. Lombardo, Appl. Catal. A: Gen. 263 (2004) 91–101.
[8] N. Muradov, Int. J. Hydrogen Energy 26 (2001) 1165–1175.
[9] (a) N.Z. Muradov, Int. J. Hydrogen Energy 18 (1993) 211;
(b) L. Piao, Y. Li, J. Chen, L. Chang, J.Y.S. Lin, Catal. Today 74 (2002) 145–155;
(c) R.A. Couttenye, M. Hoz De Vila, S.L. Suib, J. Catal. 233 (2005) 317–326.
[10] (a) E. Ruckenstein, Y.H. Hu, Carbon 3 (1998) 269–275;
(b) N. Muradov, Z. Chen, F. Smith, Int. J. Hydrogen Energy 30 (2005) 1149–1158.
[11] B.C.H. Steele, A. Heinzel, Nature 44 (2001) 342–345.
[12] Y. Li, J. Chen, L. Chang, Y. Qin, J. Catal. 178 (1998) 76–83.
[13] (a) N.M. Rodríguez, J. Mater. Res. 8 (1993) 3233;
(b) M.A. Ermakova, D.Y. Ermakov, G.G. Kuvshinov, L.M. Plyasova, J. Catal. 197 (1999) 77–84;
(c) F. Winter, V. Koot, A. Jos van Dillen, J.W. Geus, K.P. de Jong, J. Catal. 236 (2005) 91–100.
[14] (a) N.Z. Muradov, Energy Fuels 12 (1998) 41–48;
(b) D. Duprez, K. Fadili, J. Barbier, Ind. Eng. Chem. Res. 36 (1997) 3180–3187.
[15] J.I. Villacampa, C. Royo, E. Romero, J.A. Montoya, P. Del Angel, A. Monzón, Appl. Catal. A: Gen. 252 (2003) 363–383.
[16] K. Otsuka, S. Takenaka, H. Ohtsuki, Appl. Catal. A: Gen. 273 (2004) 113–124.
[17] A. Cavani, F. Trifiro, A. Vaccari, Catal. Today 11 (1991) 173–301.
[18] The Chemical Composition of Hydrotalcite and the Hydrotalcite Group of Minerals, vol. 58, W.F. Foshag, Washington, 1921, pp. 147F–153F.
[19] (a) K. Takehira, T. Shishido, P. Wang, T. Kosaka, K. Takaki, J. Catal. 221 (2004) 43–54;
(b) S. Murcia-Mascaros, R.M. Navarro, L. Gomez-Sainero, U. Costantino, M. Nocchetti, J.L.G. Fierro, J. Catal. 198 (2001) 338.
[20] (a) Y. Li, J. Chen, L. Chang, L. Chang, Appl. Catal. A: Gen. 163 (1997) 45–57;
(b) J. Chen, Y. Li, Z. Li, X. Zhang, Appl. Catal. A: Gen. 269 (2004) 179–189.
[21] U. Costantino, F. Marmottini, M. Nocchetti, R. Vivani, Eur. J. Inorg. Chem. (1998) 1439–1446.
[22] Joint Committee on Powder Diffraction Standard, International Centre for Diffraction Data, Pennsylvania, 1997.
[23] (a) S. Miyata, A. Okada, Clays Clay Miner. 25 (1977) 14–17;
(b) S. Miyata, Clays Clay Miner. 31 (1983) 305.
[24] D. Dissanayake, M.P. Rosynek, K.C.C. Kharas, J.H. Lunsford, J. Catal. 132 (1991) 117.
[25] L. Garcia, R. French, S. Czernik, E. Chornet, Appl. Catal. A: Gen. 201 (2000) 225.
[26] T. Ueckert, R. Lamber, N.I. Jaeger, U. Schubert, Appl. Catal. A: Gen. 155 (1997) 75–85.
[27] T.V. Choudhary, E. Aksoylu, D.W. Goodman, Catal. Rev. Sci. Eng. 45 (2003) 151–203.
[28] E. Ruckenstein, Y.H. Hu, Carbon 36 (1998) 269–275.
[29] A. Djaidja, S. Libs, A. Kiennemann, A. Barama, Catal. Today, in press.